Ultramicroscopy 185 (2018) 81–89

Contents lists available at ScienceDirect

Ultramicroscopy

journal homepage: www.elsevier.com/locate/ultramic

Fine electron biprism on a Si-on-insulator chip for off-axis electron holography

Martial Duchamp[a,b,*], Olivier Girard[c,d], Giulio Pozzi[b,e], Helmut Soltner[f], Florian Winkler[b], Rolf Speen[b], Rafal E. Dunin-Borkowski[b], David Cooper[c,d]

[a] School of Materials Science and Engineering, Nanyang Technological University, 50 Nanyang Avenue, Singapore 639798, Singapore
[b] Ernst Ruska-Centre for Microscopy and Spectroscopy with Electrons (ER-C) and Peter Grünberg Institute (PGI), Forschungszentrum Jülich, 52425 Jülich, Germany
[c] Université Grenoble Alpes, 38000 Grenoble, France
[d] CEA, LETI, MINATEC Campus, 38054 Grenoble, France
[e] Department of Physics and Astronomy, University of Bologna, viale B. Pichat 6/2, 40127 Bologna, Italy
[f] Central Institute of Engineering, Electronics and Analytics (ZEA-1), Forschungszentrum Jülich, 52425 Jülich, Germany

ARTICLE INFO

Article history:
Received 3 February 2017
Revised 15 November 2017
Accepted 19 November 2017
Available online 22 November 2017

ABSTRACT

Off-axis electron holography allows both the amplitude and the phase shift of an electron wavefield propagating through a specimen in a transmission electron microscope to be recovered. The technique requires the use of an electron biprism to deflect an object wave and a reference wave to form an interference pattern. Here, we introduce an approach based on semiconductor processing technology to fabricate fine electron biprisms with rectangular cross-sections. By performing electrostatic calculations and preliminary experiments, we demonstrate that such biprisms promise improved performance for electron holography experiments.

1. Introduction

Off-axis electron holography is a powerful technique that can be used to record both the amplitude and the phase shift of an electron wavefield in the transmission electron microscope (TEM) [1], as described in several books [*e.g.*, 2–4] and review papers [*e.g.*, 5,6]. The phase shift depends on both the electrostatic potential and the vertical component of the magnetic vector potential within and around the specimen, according to the Aharonov–Bohm effect [7]. Most implementations of the technique rely on the deflection of electrons that have passed through the specimen towards a vacuum reference electron wave using a Möllenstedt–Düker electron biprism, which normally takes the form of a sub-μm-diameter metal or metal-coated quartz wire [8,9] that is located close to a conjugate image plane in the microscope (in an aperture holder). As the biprism should not be placed exactly in a conjugate image plane, suitable lens excitations are required for electron holography. The phase shift can be reconstructed from a recorded electron hologram and used to provide valuable information about physical quantities such as the mean inner potential of the specimen [10], local variations in dopant potential in semiconductors [11], elementary charge distributions [12] and magnetic fields [6,13].

Despite considerable progress in many aspects of instrumentation for electron microscopy, little has been done to improve the design and manufacture of electron biprisms. In this paper, we describe a rectangular biprism geometry that can be realized using semiconductor device fabrication technology. By using this approach, the geometrical dimensions of the biprism and counter-electrodes can be chosen independently, subject to the resolution of the processing steps (see Section 3.2 below). After presenting some general considerations about the relationship between the design of an electron biprism and a recorded electron hologram in Section 2, we describe our fabrication process and illustrate its implementation in a Philips CM20 field emission gun (FEG) TEM in Section 3. We then present calculations of the electrostatic potential generated by the new rectangular electron biprism in Section 4 and characterize it experimentally by recording both vacuum reference and sample electron holograms in Section 5.

* Corresponding author at: School of Materials Science and Engineering, Nanyang Technological University, 50 Nanyang Avenue, Singapore 639798, Singapore.
E-mail address: mduchamp@ntu.edu.sg (M. Duchamp).

https://doi.org/10.1016/j.ultramic.2017.11.012

2. General considerations

The phase resolution in a phase image recorded using off-axis electron holography is related directly to the contrast of the holographic interference fringes, which is in turn determined primarily by two competing factors: the transverse spatial coherence of the electron source and the electron dose [14]. Improvements in phase resolution have been achieved by using brighter electron sources [15] and cylindrical illumination [16], by improving microscope stability (thereby allowing longer exposure times) [17] and recently by using direct electron detectors [18]. However, additional considerations are related to the geometry and stability of the electron biprism, whose design is traditionally based on a thin metal or metal-coated quartz wire, which is located between two grounded plates and has a voltage applied to it.

The reason why a small biprism diameter is important results from the following considerations. For a small, incoherent circular electron source of uniform intensity, a measure of the size of the lateral coherence patch x_1 is given by the equation

$$x_1 = \lambda/\alpha, \tag{1}$$

where α is the angle subtended by the source and λ is the electron wavelength [19]. The value of x_1 provides an approximate indication of the separation of two points, between which interference effects are observable. The use of a large biprism diameter means that the most coherent parts of the electron wave are absorbed by the biprism and cannot be overlapped with each other, resulting in lower hologram fringe contrast. The width of the overlap region is given by the equation

$$w_{hol} = \frac{2\gamma|b|f_{obj}}{|a+b|} - \frac{2rf_{obj}}{a}, \tag{2}$$

where a and b are geometrical distances related to the position of the biprism in the electron optical setup, f_{obj} is the focal lens of the imaging (objective) lens, γ is the deflection angle (which is proportional to the voltage applied to the biprism) and r is the radius of the biprism [20]. Eqs. (1) and (2) show how the radius of the biprism affects the width of the overlap region w_{hol} for a given applied voltage and electron optical configuration and hence the achievable interference fringe contrast for a given value of w_{hol}. The radius of the biprism can also have an influence on vignetting effects (Eq. 12 in Ref. [21]).

To a first approximation, the electrostatic potential distribution near a biprism can be approximated by the electrostatic potential distribution of a cylindrical capacitor, which is described by the equation

$$U(R) = U_f \frac{\ln(R/R_a)}{\ln(r/R_a)}, \tag{3}$$

where R is the position of the electron beam from the centre of the biprism, r is the radius of the biprism, U_f is the potential applied to the biprism and R_a is the outer capacitor plate radius [8]. However, such a plate capacitor does not provide a good model for a realistic electron biprism, for which the position and geometry of the counter-electrode may not be well-defined. It is also not suitable for calculating the potential for other biprism and counter-electrode geometries.

A technique that is commonly used to manufacture electron biprisms involves manually drawing a thin glass fibre from a quartz or silica rod above a hydrogen-oxygen flame [8]. The resulting biprism typically has a surface roughness in the nm range and a diameter of approximately 0.5 µm. However, the diameters of such biprisms can vary by up to several hundred nm between successive preparations. Moreover, the conductivity of the glass filament has to be improved by depositing a thin layer of metal, which can then be sputtered off by the electron beam during use, leading to the formation of dielectric patches that can charge up in the presence of the electron beam (affecting the interference pattern) or to the disruption of the conductivity of the biprism, such that it no longer functioning properly. Some of these drawbacks can be avoided by the use of a Wollaston Pt wire [22,23]. However, contamination of the wire due to its prolonged use may still require its replacement. At the highest accelerating voltage that we have used (300 kV), a biprism that has a circular cross-section is not always completely opaque to electrons. Furthermore, as a result of the build-up of charge in its insulating core and poor conductivity of its coating, it can charge up during long (several hour) observations, such that at the end of a working day its Fresnel image with no external bias applied reveals the presence of residual charge (corresponding to a few volts of applied voltage). This effect usually disappears overnight. Even though it does not affect electron holography observations that are carried out on timescales of seconds or minutes, it can result in irreproducible imaging conditions.

Although this technology for fabricating biprisms has dominated the field of electron interferometry and holography, its use is affected by the practical shortcomings described above. In order to circumvent some of these problems, Ogai et al. reported the fabrication of Al filaments on Si nitride membranes using a focused ion beam [24]. However, the additional scattering of electrons by the Si nitride membrane reduced the benefits of using thinner filaments and the more controlled fabrication process. Nakamatsu et al. reported the use of 80 nm-diameter filaments of diamond-like C bridged between two electrodes [25] and observed an increase in fringe contrast when compared to the use of a conventional biprism. However, the geometry of the filament was difficult to control. Recently, the glass filament method was improved by using a computer-controlled fibre-pulling system, resulting in a reproducible biprism diameter of ~400 nm [26].

The use of a rectangular biprism reduces many of these shortcomings, because (i) its longitudinal thickness can be made large enough to be completely opaque to electrons, (ii) all of the biprism is made from the same material, preventing its charging and contact potential differences between the electrodes that can lead to charging of the wire, (iii) the use of highly-doped Si allows contamination to be removed using standard cleaning techniques, meaning that its lifetime can be longer than that of a conventional biprism, and (iv) many identical biprisms can be fabricated together at the same time using standard semiconductor fabrication processes.

It should be noted that parameters such as the contrast in an electron hologram and the width of the interference region where the object wave and reference wave overlap are highly dependent on the electron optical configuration and stability of the TEM that is being used. Therefore, the characterization of an electron biprism by recording electron holograms must be performed for each specific TEM on which it is mounted. In contrast, the accurate modelling of electrostatic fields around a biprism, as described below, is independent of the TEM stability and the electron optical configuration.

3. Fabrication and implementation of a rectangular biprism in a TEM

3.1. Concept of a rectangular biprism on a Si-on-insulator chip

The rectangular electron biprism that we describe here is fabricated from a Si-on-insulator (SOI) wafer, which comprises a conducting doped single crystalline Si layer on a non-conducting amorphous SiO_2 layer on a Si substrate. The biprism, the counter-electrodes and all of the other required electrical lines are patterned from the top Si layer using standard semiconductor

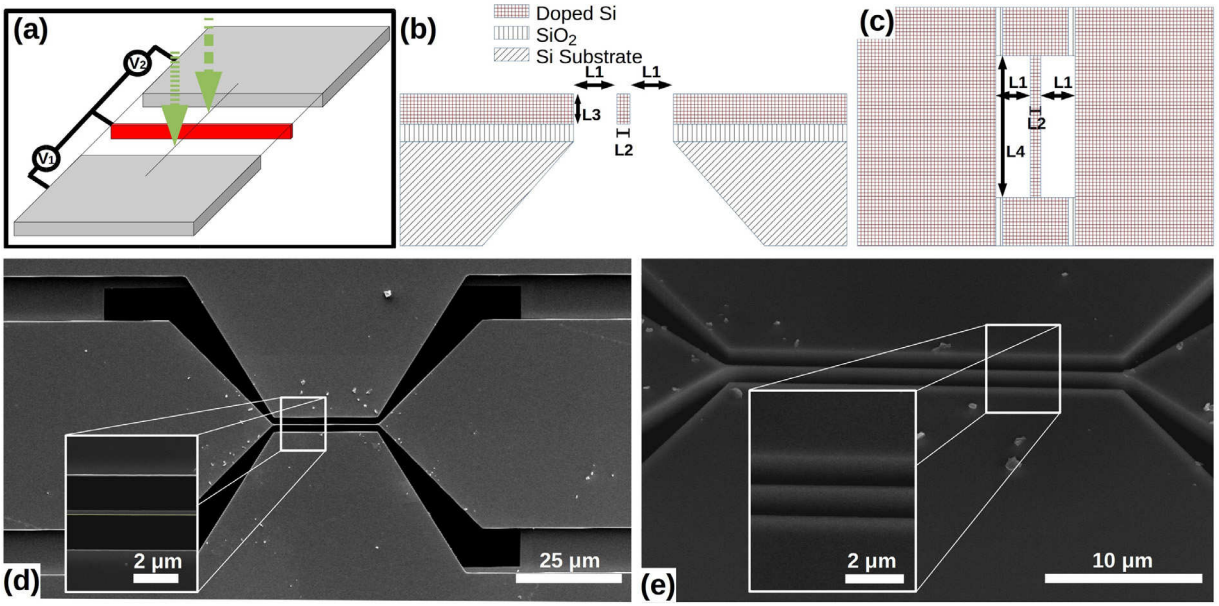

Fig. 1. (a) Schematic drawing of a rectangular biprism between two electrodes. (b) Cross-section and (c) top view of a rectangular biprism with biprism-to-electrode spacing L_1, width L_2 and length L_4. The cross-section shows the inner electrode of height L_3. (d) Top view and (e) tilted (52°) view scanning electron micrographs of a rectangular biprism, for which $L_1 = 2\,\mu m$, $L_2 = 120\,nm$, $L_3 = 750\,nm$ and $L_4 = 30\,\mu m$. The insets in (d) and (e) show higher magnification scanning electron micrographs of the 120 nm-wide biprism.

processing technology. The free-standing biprism and counter-electrodes are isolated electrically from each other by patterning empty trenches in the Si layer. By using this approach, both the rectangular biprism and the counter-electrodes are all in the same plane, as shown in Fig. 1a. Moreover, independent control of all of the dimensions is possible, including the parameters L_1 (biprism to counter-electrode spacing), L_2 (biprism width), L_3 (biprism and counter-electrode height) and L_4 (biprism length), as shown in Fig. 1b and c. The fabrication process allows biprism widths L_2 as small as ~100 nm to be achieved. The thickness L_3 of the top Si layer, which is typically between 500 nm and a few µm, has a direct influence on the minimum achievable value of L_2. The thickness of the SiO_2 isolating layer can also be chosen according to the requirements for electrical isolation between the top Si layer and the Si substrate.

3.2. Fabrication

The first photolithographic step involves defining the biprism, counter-electrodes and electrical lines in the top Si layer. The surrounding regions are removed by etching the top Si layer down to the SiO_2. The remaining top Si layer is then oxidized, in order to protect it during opening of the substrate. The second photolithographic step involves opening the back side of the substrate by etching away the Si, making use of alignment marks in the top Si layer. The final step involves removing the sacrificial SiO_2 layer. In this way, the rectangular biprism is left freely suspended and fixed at its ends, with a length that can be controlled between a few µm and more than 100 µm. The larger Young's modulus of Si compared to that of glass and the shorter suspended length and cross-sectional shape of the rectangular biprism contribute to its improved mechanical stability.

Completed biprisms were checked using scanning electron microscopy (SEM). Fig. 1d and e show top view secondary electron images of a representative biprism chip that has been cut from its wafer. The white spots, which are residues from the cutting process, do not have a noticeable impact on the performance of the device. The dimensions of the device that is shown in Fig. 1d and e are $L_1 = 2\,\mu m$, $L_2 = 120\,nm$, $L_3 = 750\,nm$ and $L_4 = 30\,\mu m$.

3.3. Implementation in a Philips CM20 FEG TEM

A dedicated chip holder was designed, machined and used to test the biprism in the selected area (SA) aperture plane of a Philips CM20 FEG TEM. The holder was designed to accommodate a 10 mm × 3 mm chip, which was fixed into the holder at one end using an M3 open screw and at the other end by four needles that were used to provide electrical connections to the device. A design drawing of the holder is shown in Fig. 2a. We did not encounter any major technical issues in the development of this aperture rod. For columns from other TEM manufacturers, the implementation of such a biprism simply requires the development of a new aperture rod and possibly a new aperture drive mechanism. The inset in Fig. 2a shows a bright-field micrograph of the biprism inserted in the SA aperture plane of the microscope. Fig. 2b shows a vacuum reference electron hologram recorded using a 3 s exposure time with a 27 V bias applied to the biprism shown in Fig. 1d and e. The hologram shown in Fig. 2b has as an overlap width of 45 nm, an interference fringe spacing of 0.2 nm and an interference fringe contrast of 16% measured by dividing the difference between the maximum and minimum intensity of the interference fringes by the sum of the maximum and minimum intensity at the centre of the hologram.

4. Electrostatic calculations

4.1. Analytical calculations

We first present two-dimensional analytical calculations of the electrostatic potential for a biprism that is infinitely long in the direction parallel to its axis, with counter-electrodes that take the form of infinite planes. In order to model the rectangular shape of the biprism, we extended a method that had previously been used to approximate a cylindrical wire by a collection of line charges [27]. We begin with an analytical expression for the potential of an infinitely long wire between two parallel planes [28]. A rectangular lattice of such wires is assumed, with the positions and magnitudes of the surface charge densities chosen in such a way that the potential at intermediate points is constant. In this way, one

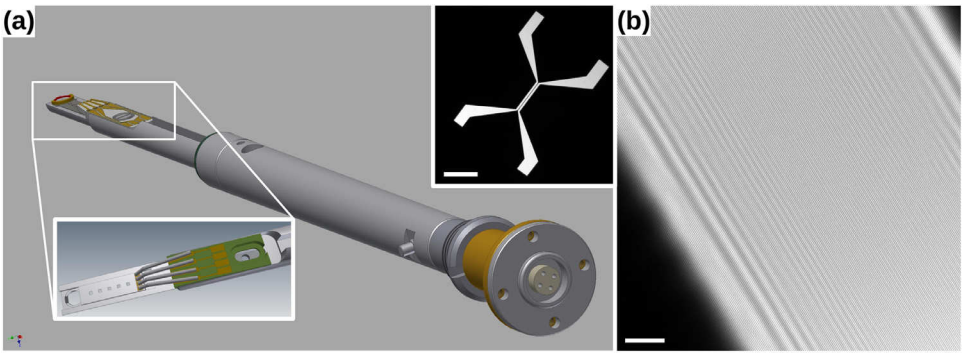

Fig. 2. (a) Model of an aperture rod that was designed to accommodate an electrically contacted chip containing the biprism in the selected area (SA) plane of the microscope. The inset shows an image of the biprism recorded in focus in the SA plane of a Philips CM20 FEG TEM. (b) Vacuum reference off-axis electron hologram recorded at 200 kV in a Philips CM20 FEG TEM with 27 V applied to the rectangular biprism shown in Fig. 1d and e under standard imaging conditions. The exposure time was 3 s and the scale bar is 5 nm. The scale bar in the inset is 30 µm.

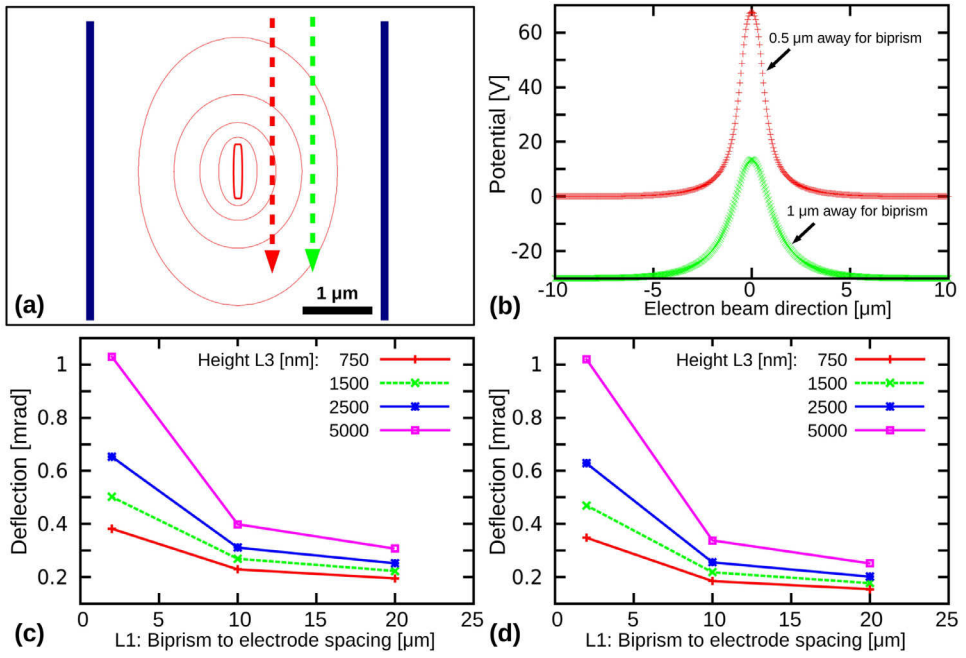

Fig. 3. Two-dimensional analytical electrostatic calculations performed for a rectangular biprism geometry for electrodes that are infinitely long perpendicular to the electron beam direction with a bias of 100 V applied between the biprism and the counter-electrodes. (a) Equipotential contours calculated for a 750 nm-high, 120 nm-wide rectangular biprism located 2 µm from each counter-electrode with an applied bias of 100 V. The spacing of the contour lines is 20 V. The dashed arrows mark the electron beam trajectories considered in (b). (b) Line profiles showing the electrostatic potential experienced by an electron beam travelling at distances of 0.5 and 1 µm from the biprism marked in (a). The line profile has been displaced vertically downwards for clarity. (c,d) Deflections experienced by a 200 kV electron beam for different rectangular biprism geometries that have heights (L_3) of between 750 and 5000 nm, biprism-to-electrode spacings (L_1) of 2–20 µm and biprism widths (L_2) of (c) 120 and (d) 250 nm.

of the equipotential lines that encloses all of the charged lines approximates the desired rectangular cross-section very closely, with the calculation improving as the number of charged lines is increased. An advantage of this model is that the electron optical phase shift and the deflection of the incident electron beam can be expressed in analytical form in the high energy approximation [29,30].

Fig. 3 shows the result of analytical calculations performed for a potential of 100 V at the surface of the biprism shown in Fig. 1d and e, with the counter-electrodes at 0 V. Fig. 3a shows equipotential contours in the vacuum region around the biprism. The contours are clearly elongated in the electron beam direction. Fig. 3b shows the magnitude of the electrostatic potential calculated along the trajectory of an electron beam that travels at a distance of 0.5 or 1 µm from the biprism wire (assuming that is not deflected). It should be noted that only the electric field in the transverse direction contributes to the deflection of the electron beam. Fig. 3c and d show the influence of the height of the biprism on the deflection angle experienced by an incident electron. For simplicity, the transverse electric field was integrated in the electron beam direction at a given distance from the biprism (again neglecting its transverse displacement). The deflection angle was then determined for a 200 kV electron beam. The three geometrical parameters that were used to specify the two-dimensional biprism geometry were varied and the deflection angle was plotted as a function of biprism-to-electrode spacing. Fig. 3c and d show the results of these calculations for biprism widths L_2 of 120 and 250 nm, respectively and for different biprism heights L_3. The figures show that the width of the biprism has little influence on the deflection angle. In contrast, the influence of the height of the biprism is significant and results in a linear increase in deflection angle of approximately 0.15 mrad for each µm of height for a biprism to counter-electrode distance of 2 µm. An increase in biprism-to-electrode spacing decreases the deflection angle. In order to compare the results with those for a cylindrical biprism geometry, we performed similar calculations for the classical configuration

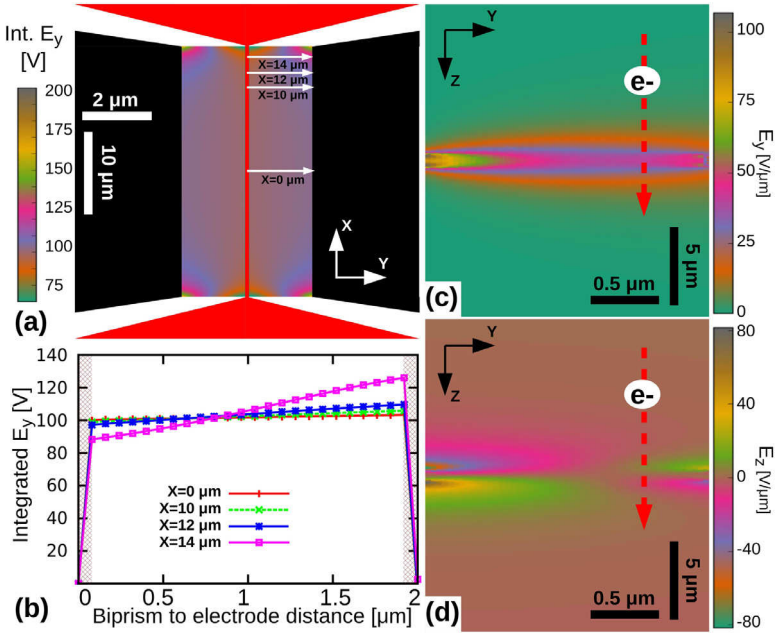

Fig. 4. Boundary element calculations calculations of the electric field for a rectangular biprism geometry for a 100 V bias applied between the biprism and the counter-electrodes for $L_1 = 2\,\mu m$, $L_2 = 120\,nm$, $L_3 = 750\,nm$ and $L_4 = 30\,\mu m$. (a) Transverse electric field E_y integrated in the electron beam direction. The black areas are the counter-electrodes. The red areas are the biprism and the electrical connections to it, all of which are at a bias of 100 V with respect to the counter-electrodes. The arrows mark the positions of the line profiles plotted in (b). (b) Line profiles of the transverse electric field E_y integrated in the electron beam direction shown in (a), displayed along the lines marked by arrows. (c,d) Cross-sectional two-dimensional calculations of the electric field in the electron beam direction z at the centre of the biprism (corresponding to the line at $x = 0$ marked in (a)) for (c) the transverse field E_y and (d) the vertical field E_z. Note the different horizontal and vertical scale bars. The dashed arrows mark the electron beam trajectories.

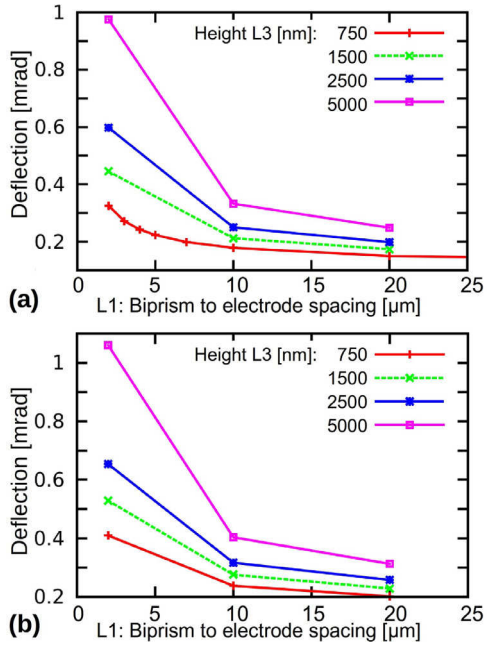

Fig. 5. Deflections experienced by the electron beam at 200 kV for different rectangular biprism geometries obtained from boundary element calculations for a 100 V bias applied between the biprism and the counter-electrodes, for heights (L_3) of between 750 and 5000 nm, biprism-to-electrode spacings (L_1) of 2–20 µm and biprism widths (L_2) of (a) 120 and (b) 250 nm.

with a biprism-to-electrode spacing of 2 mm and obtained deflection angles of between 0.1 and 0.15 mrad for biprism diameters of 100 nm to 1.5 µm, respectively. These deflection angles calculated for a conventional biprism should be compared with the value of 0.38 mrad obtained for the biprism shown in Fig. 1d and e, which suggest that larger deflection angles can be obtained by using the present biprism design.

4.2. Numerical calculations

Boundary element method (BEM) calculations were used to simulate the electrostatic potential of a real device, with 100 V applied between the rectangular biprism and the counter-electrodes, using the program Coulomb from the company IES (Integrated Engineering Software; https://www.integratedsoft.com/product/coulomb/). A mesh was generated with a higher density of elements only where needed and a coarser mesh was used where the element density was not as critical. The geometry used in the calculation included the contacts to the biprism and the counter-electrodes, which produce fringing fields. Fig. 4a shows a projection of the transverse electric field in the electron beam direction. The integrated transverse electric field is homogeneous along the length of the biprism, except near its ends. Fig. 4b shows plots of the integrated transverse electric field at four different distances along the length of the biprism. The plots suggest that approximately 80% of the length of the biprism has a constant integrated transverse electric field and can be used to record off-axis electron holograms experimentally. Fig. 4c and d show cross-sections of the transverse and vertical electric field amplitudes in the central plane of the biprism. The plots show the distribution of the fringing field around the biprism and the counter-electrodes.

The total deflection angles were again calculated by integrating the transverse electric field in the electron beam direction (neglecting the transverse displacement of the electron beam) for an accelerating voltage of 200 kV, as shown in Fig. 5. They can be compared directly with the deflection angles reported in Fig. 3c and d, as all of the parameters are identical between the two calculations, apart from the finite length of the biprism and the finite length and height of the electrodes. A larger biprism again results in a slightly smaller deflection angle. The deflection angles

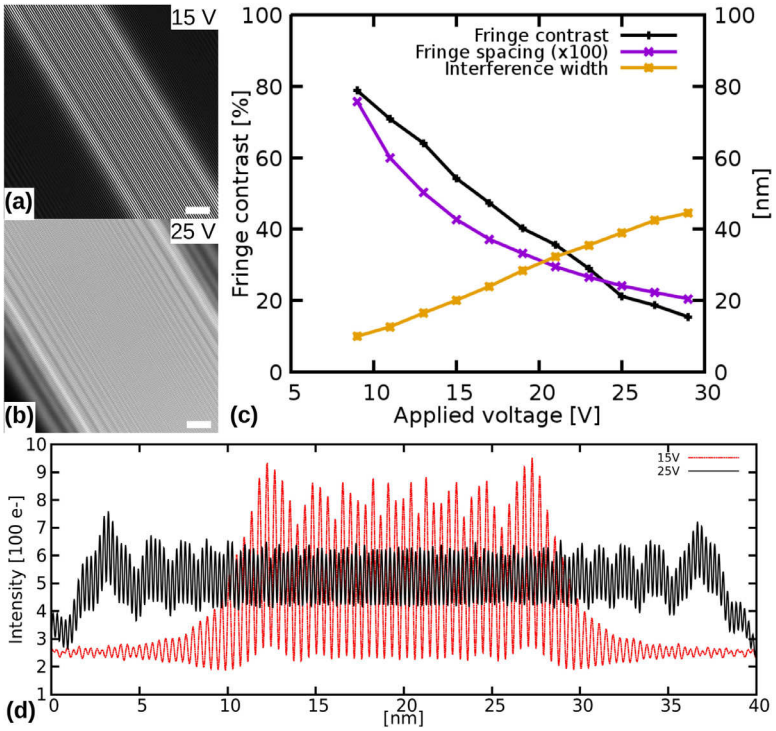

Fig. 6. (a,b) Off-axis electron holograms recorded for biprism voltages of 15 and 25 V, respectively, with a voltage applied between the rectangular biprism and two counter-electrodes, recorded at 200 kV in a Philips CM20 FEG TEM with the biprism close to the SA aperture image plane. The biprism is shown in Fig. 1. The scale bar is 5 nm. (c) Interference fringe contrast, interference fringe spacing and overlap width plotted as a function of applied voltage. (d) Line profiles showing the intensity perpendicular to the biprism in the holograms shown in (a) and (b).

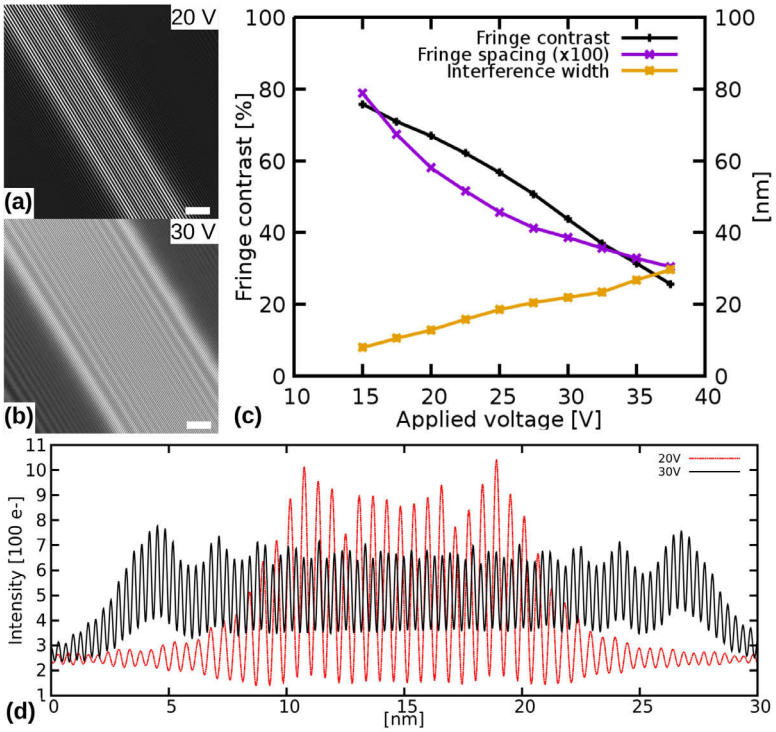

Fig. 7. (a,b) Off-axis electron holograms recorded for biprism voltages of 15 and 25 V, respectively, with a voltage applied between the rectangular biprism and one of the two counter-electrodes, with the second counter-electrode at the same voltage as the biprism. The holograms were recorded at 200 kV in a Philips CM20 FEG TEM with the biprism close to the SA aperture image plane. The biprism is shown in Fig. 1. The scale bar is 5 nm. (c) Interference fringe contrast, interference fringe spacing and overlap width plotted as function of the voltage applied between the rectangular biprism and one of the two counter-electrodes, with the second counter-electrode at the same voltage as the biprism. (d) Line profiles showing the intensity perpendicular to the biprism in the holograms shown in (b) and (c).

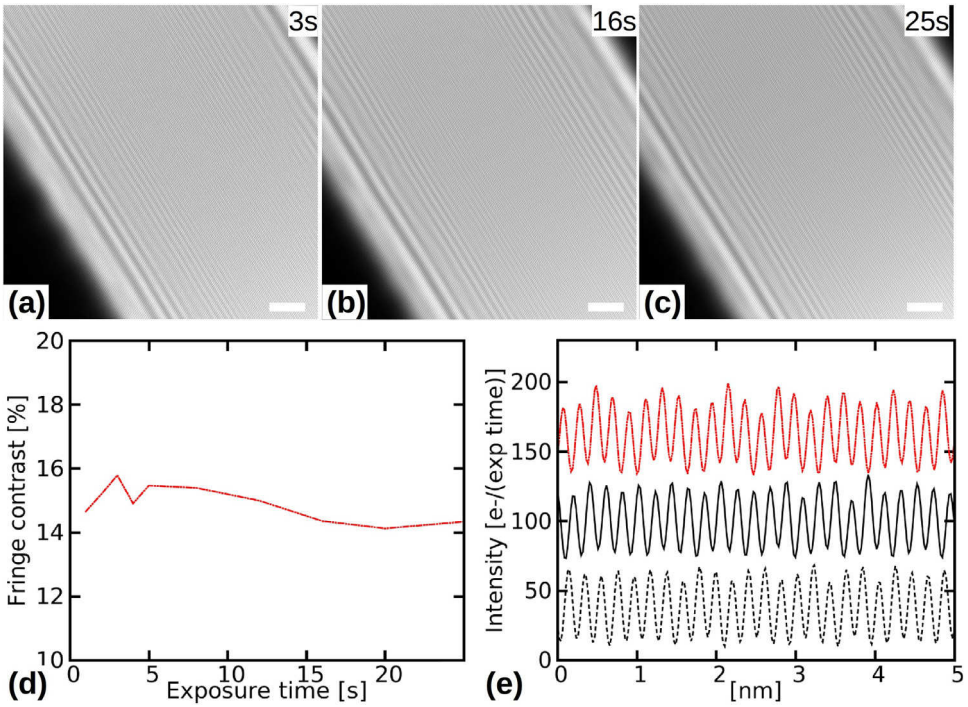

Fig. 8. Off-axis electron holograms recorded at 200 kV in a Philips CM20 FEG TEM for a 27 V bias applied between the biprism and the counter-electrodes for acquisition times of (a) 3, (b) 16 and (c) 25 s. The biprism is shown in Fig. 1d. (d) Interference fringe contrast plotted as a function of exposure time. (e) Line profiles showing the intensity perpendicular to the biprism close to the middle of the holograms shown in (a-c) for acquisition times of 3 s (top), 16 s (middle) and 25 s (bottom). The curves have been shifted downwards vertically for better visibility.

are slightly lower than those calculated using the analytical expressions, as a result of the more confined field in the beam direction due to the finite height of the counter-electrodes in the numerical calculation. Larger deflection angles can again be obtained by increasing the biprism height or decreasing the biprism-to-electrode spacing. Although both options are technically possible, increasing the biprism height requires overgrowth of epitaxial doped Si onto the top Si surface, which is more time-consuming than changing the biprism-to-electrode spacing during patterning of the top Si layer.

5. Preliminary experiments in a Philips CM20 FEG TEM

Our biprism structures were fabricated from a SOI wafer with a standard 750 nm-thick top SiO_2 layer. We chose a biprism-to-electrode spacing of 2 µm to perform preliminary electron holography experiments, as described below.

5.1. Conventional biprism configuration

In Section 3.3, we described the experimental setup used to introduce an electrically contacted biprism system in the SA aperture plane of a CM20 FEG TEM. In this section, we varied the voltage applied to the biprism and kept the counter-electrodes at ground potential. For each applied voltage, we recorded an off-axis electron hologram from vacuum alone and measured the overlap width, interference fringe spacing and interference fringe contrast. Fig. 6c shows these parameters plotted as a function of applied voltage for the biprism shown in Fig. 1d and e. The behaviour of the rectangular biprism can be seen to follow the typical characteristics of cylindrical biprisms, with a linear increase in overlap width and a decrease in interference fringe spacing and interference fringe contrast with applied voltage. In the present setup, the maximum voltage that could be applied to the biprism was limited by the small biprism-to-electrode spacing of 2 µm, as shadowing by the counter-electrodes then became a problem at higher applied voltages. This limitation can easily be overcome by using a larger biprism-to-electrode spacing. For an applied voltage of 27 V, an overlap width of 45 nm, an interference fringe spacing of 0.2 nm and an interference fringe contrast of 16% were measured. These values are better than those previously reported under similar experimental conditions for a 0.5 nm interference fringe spacing and a 35 nm overlap width [31]. Representative off-axis electron holograms recorded from vacuum alone are shown in Fig. 6a and b for biprism voltages of 15 and 25 V, respectively. Corresponding line profiles are shown in Fig. 6d.

5.2. Single-electrode biprism configuration

An additional feature of our biprism design is the possibility to independently assign different potentials to the counter-electrodes and the biprism. A similar study to that performed in Section 5.1 was carried out with one counter-electrode kept at the biprism potential. In this case, one side of the biprism setup does not deflect the electron beam, while the other side deflects the beam as in a usual biprism system. For this configuration, the maximum voltage that could be applied to the system was greater than 35 V before shadowing by the counter-electrode became a problem. Fig. 7c shows the overlap width, interference fringe spacing and interference fringe contrast plotted as function of applied voltage. A hologram recorded with 35 V applied between the biprism and only one electrode results in a similar image to that obtained previously with 17 V applied between the biprism and both electrodes, *i.e.*, 38 and 0.32 nm for the interference width and interference fringe spacing, respectively. It is interesting to note the interference fringe contrast is 40% with two electrodes grounded, but only 30% when one electrode is kept at the biprism potential. Representative off-axis electron holograms recorded from vacuum alone are shown in Fig. 7a and b for biprism voltages of 20 and 30 V, respectively. Corresponding line profiles are shown in Fig. 7d.

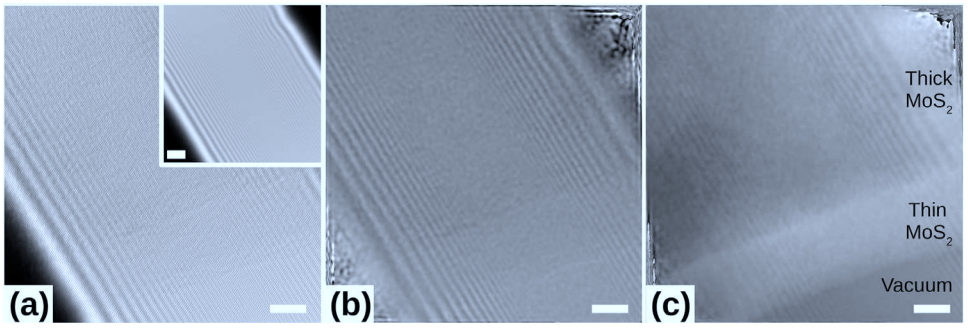

Fig. 9. (a) Off-axis electron hologram of an MoS_2 multilayer flake recorded at 200 kV in a Philips CM20 FEG TEM with 27 V applied to the rectangular biprism, with a vacuum reference electron hologram shown in the inset. The biprism is shown in Fig. 1. (b,c) Reconstructed amplitude and phase images, respectively. The scale bar is 5 nm.

5.3. Stability

As mentioned above, the phase resolution can be improved by increasing the biprism stability during the recording of an off-axis electron hologram, as any instability in the biprism results in a loss of interference fringe contrast. Figs. 8a–c show three electron holograms recorded using acquisition times of 3, 16 and 25 s with 27 V applied to the biprism and both counter-electrodes kept at ground potential. The variation in fringe contrast over time, which is a measure of the stability of both the microscope and the biprism, is shown in Fig. 8d. Corresponding line profiles of the holographic fringes are shown in Fig. 8e. The contrast only decreases from 15% to 14% for exposure times of up to 25 s, confirming the stability of the rectangular biprism system.

5.4. Preliminary results on an MoS_2 specimen using a rectangular biprism

Fig. 9a shows a representative off-axis electron hologram of the edge of a few-monolayer-thick MoS_2 flake recorded using the rectangular biprism shown in Fig. 1. The corresponding reconstructed amplitude and phase are shown in Fig. 9b and c. The phase image demonstrates that the rectangular biprism can be applied successfully to study samples of current interest [10].

6. Outlook

In this paper, we have described the design of an electron biprism that has a rectangular cross-section and counter-electrodes in the same plane and its successful fabrication using semiconductor device processing technology. The flexibility of the fabrication process provides significant freedom in choosing the biprism dimensions, including the biprism-to-electrode spacing, the biprism width, the biprism height and the biprism length. Electrostatic calculations have been performed to understand the influence of the biprism geometry on the deflection of the electron beam. The performance of the biprism in the SA aperture plane of a CM20 FEG TEM has been demonstrated. In addition to its flexibility, the technology that we describe promises to provide easy (and ultimately cheap) access to both conventional and more complicated electrode geometries for a wide range of interferometry experiments in the TEM.

Acknowledgment

The research leading to these results has received funding from the European Research Council under the European Union's Seventh Framework Programme (FP7/2007-2013)/ERC grant agreement number 320832.

Supplementary materials

Supplementary material associated with this article can be found, in the online version, at doi:10.1016/j.ultramic.2017.11.012.

References

[1] D. Gabor, A new microscopic principle, Nature 161 (1948) 777–778, doi:10.1038/161777a0.
[2] A. Tonomura, L.F. Allard, G. Pozzi, D.C. Joy, Y.A. Ono, Electron holography, in: Proceedings of the International Workshop On Electron Holography, Holiday Inn World's Fair, Knoxville, Tennessee, USA, August 29-31, 1994, Elsevier, New York, 1995. http://isbnplus.org/9780444820518.
[3] A. Tonomura, Electron Holography, Springer, Berlin, Heidelberg, 1999 http://link.springer.com/10.1007/978-3-540-37204-2 (accessed November 1, 2016).
[4] E. Völkl, L.F. Allard, D.C. Joy, Introduction to Electron Holography, Springer, US, Boston, MA, 1999 http://link.springer.com/10.1007/978-1-4615-4817-1 (accessed November 1, 2016).
[5] H. Lichte, M. Lehmann, Electron holography—basics and applications, Rep. Prog. Phys. 71 (2008) 016102, doi:10.1088/0034-4885/71/1/016102.
[6] P.A. Midgley, R.E. Dunin-Borkowski, Electron tomography and holography in materials science, Nat. Mater. 8 (2009) 271–280, doi:10.1038/nmat2406.
[7] Y. Aharonov, D. Bohm, Significance of electromagnetic potentials in the quantum theory, Phys. Rev. 115 (1959) 485–491, doi:10.1103/PhysRev.115.485.
[8] G. Möllenstedt, H. Düker, Beobachtungen und Messungen an Biprisma-Interferenzen mit Elektronenwellen, Z. Für Phys. 145 (1956) 377–397, doi:10.1007/BF01326780.
[9] G. Möllenstedt, H. Düker, Fresnelscher Interferenzversuch mit einem Biprisma für Elektronenwellen, Naturwissenschaften 42 (1955) 41–41, doi:10.1007/BF00621530.
[10] F. Winkler, A.H. Tavabi, J. Barthel, M. Duchamp, E. Yucelen, S. Borghardt, B.E. Kardynal, R.E. Dunin-Borkowski, Quantitative measurement of mean inner potential and specimen thickness from high-resolution off-axis electron holograms of ultra-thin layered WSe_2, Ultramicroscopy 178 (2017) 38–47, doi:10.1016/j.ultramic.2016.07.016.
[11] D. Cooper, F. de la Peña, A. Béché, J.-L. Rouvière, G. Servanton, R. Pantel, P. Morin, Field mapping with nanometer-scale resolution for the next generation of electronic devices, Nano Lett. 11 (2011) 4585–4590, doi:10.1021/nl201813w.
[12] C. Gatel, A. Lubk, G. Pozzi, E. Snoeck, M. Hÿtch, Counting elementary charges on nanoparticles by electron holography, Phys. Rev. Lett. 111 (2013) 025501, doi:10.1103/PhysRevLett.111.025501.
[13] A. Kovács, Z.-A. Li, K. Shibata, R.E. Dunin-Borkowski, Lorentz microscopy and off-axis electron holography of magnetic skyrmions in FeGe, Resolut. Discov. (2016) 1–7, doi:10.1556/2051.2016.00037.
[14] S.L.Y. Chang, C. Dwyer, C.B. Boothroyd, R.E. Dunin-Borkowski, Optimising electron holography in the presence of partial coherence and instrument instabilities, Ultramicroscopy 151 (2015) 37–45, doi:10.1016/j.ultramic.2014.11.019.
[15] M. Linck, B. Freitag, S. Kujawa, M. Lehmann, T. Niermann, State of the art in atomic resolution off-axis electron holography, Ultramicroscopy 116 (2012) 13–23, doi:10.1016/j.ultramic.2012.01.019.
[16] M. Lehmann, Influence of the elliptical illumination on acquisition and correction of coherent aberrations in high-resolution electron holography, Ultramicroscopy 100 (2004) 9–23, doi:10.1016/j.ultramic.2004.01.005.
[17] D. Cooper, R. Truche, P. Rivallin, J.-M. Hartmann, F. Laugier, F. Bertin, A. Chabli, J.-L. Rouvière, Medium resolution off-axis electron holography with millivolt sensitivity, Appl. Phys. Lett. 91 (2007) 143501, doi:10.1063/1.2794006.
[18] S.L.Y. Chang, C. Dwyer, J. Barthel, C.B. Boothroyd, R.E. Dunin-Borkowski, Performance of a direct detection camera for off-axis electron holography, Ultramicroscopy 161 (2016) 90–97, doi:10.1016/j.ultramic.2015.09.004.
[19] J.M. Cowley, Imaging and diffraction, 3rd chapter, in: J.M. Cowley (Ed.), Diffraction Physics, third revised ed., North-Holland, Amsterdam, 1995, pp. 51–73. http://www.sciencedirect.com/science/article/pii/B9780444822185500055.

[20] H. Lichte, Electron holography: optimum position of the biprism in the electron microscope, Ultramicroscopy 64 (1996) 79–86, doi:10.1016/0304-3991(96)00017-4.
[21] H. Lichte, D. Geiger, A. Harscher, E. Heindl, M. Lehmann, D. Malamidis, A. Orchowski, W.-D. Rau, Artifacts in electron holography, Ultramicroscopy 64 (1996) 67–77, doi:10.1016/0304-3991(96)00018-6.
[22] A. Ohshita, H. Teraoka, H. Tomita, Production of central electrode of electron biprism using ion beam thinning technique, Ultramicroscopy 12 (1983) 247–250, doi:10.1016/0304-3991(83)90266-8.
[23] G. Matteucci, On use of a Wollaston wire in a Möllenstedt–Düker electron biprism, J. Microsc. Spectrosc. Electron. 3 (1978) 69–71.
[24] K. Ogai, Y. Kimura, R. Shimizu, K. Ishibashi, Y. Aoyagi, S. Namba, Microfabricated submicron al-filament biprism as applied to electron holography, Jpn. J. Appl. Phys. 30 (1991) 3272, doi:10.1143/JJAP.30.3272.
[25] K. Nakamatsu, K. Yamamoto, T. Hirayama, S. Matsui, Fabrication of fine electron biprism filament by free-space-nanowiring technique of focused-ion-beam + chemical vapor deposition for accurate off-axis electron holography, Appl. Phys. Express 1 (2008) 117004, doi:10.1143/APEX.1.117004.
[26] G. Schütz, A. Rembold, A. Pooch, S. Meier, P. Schneeweiss, A. Rauschenbeutel, A. Günther, W.T. Chang, I.S. Hwang, A. Stibor, Biprism electron interferometry with a single atom tip source, Ultramicroscopy 141 (2014) 9–15, doi:10.1016/j.ultramic.2014.02.003.
[27] D.J. Griffiths, Y. Li, Charge density on a conducting needle, Am. J. Phys. 64 (1996) 706–714, doi:10.1119/1.18236.
[28] E. Durand, Electrostatique et Magnétostatique, Masson et Cie, 1953.
[29] G. Matteucci, F.F. Medina, G. Pozzi, Electron-optical analysis of the electrostatic Aharonov–Bohm effect, Ultramicroscopy 41 (1992) 255–268, doi:10.1016/0304-3991(92)90205-X.
[30] G. Pozzi, Particles and Waves in Electron Optics and Microscopy, in: P.W. Hawkes (Ed.), Advances in Imaging and Electron Physics, vol. 194, Elsevier, Academic Press, New York, NY, 2016 http://www.sciencedirect.com/science/bookseries/10765670/194.
[31] J. Cantu-Valle, F. Ruiz-Zepeda, F. Mendoza-Santoyo, M. Jose-Yacaman, A. Ponce, Calibration for medium resolution off-axis electron holography using a flexible dual-lens imaging system in a JEOL ARM 200F microscope, Ultramicroscopy 147 (2014) 44–50, doi:10.1016/j.ultramic.2014.06.003.